Chinese Journal of
POLYMER SCIENCE

RESEARCH ARTICLE

https://doi.org/10.1007/s10118-024-3200-y
Chinese J. Polym. Sci. **2024**, *42*, 1802–1810

Doping Effect of Poly(vinylidene fluoride) on Carbon Nanofibers Deduced by Thermoelectric Analysis of Their Melt Mixed Films

A. J. Paleo[a*], V. M. Serrato[b,c], J. M. Mánuel[d], O. Toledano[e,f], E. Muñoz[g], M. Melle-Franco[e], B. Krause[h], P. Pötschke[h], and K. Lozano[i]

[a] *2C2T-Centre for Textile Science and Technology, University of Minho, Campus de Azurém, 4800-058 Guimarães, Portugal*
[b] *Florida Institute of Technology, Melbourne, FL 32901, USA*
[c] *The Aerospace Corporation, El Segundo, CA 90245, USA*
[d] *Department of Condensed Matter Physics and Institute of Research on Electron Microscopy and Materials (IMEYMAT), Faculty of Sciences, University of Cádiz, Puerto Real, 11510 Cádiz, Spain*
[e] *CICECO – Aveiro Institute of Materials, Department of Chemistry, University of Aveiro, 3810-193 Aveiro, Portugal*
[f] *UNED-Universidad Nacional de Educación a Distancia, Av. de Esparta, s/n, 28232, Las Rozas, Madrid, Spain*
[g] *Facultad de Física, Pontificia Universidad Católica de Chile, Santiago, 7820436, Chile*
[h] *Leibniz-Institut für Polymerforschung Dresden e.V. (IPF), Hohe Str. 6, 01069 Dresden, Germany*
[i] *Department of Mechanical Engineering, University of Texas Rio Grande Valley, Edinburg TX 78539, USA*

Electronic Supplementary Information

Abstract The effect of temperature on the electrical conductivity (σ) and Seebeck coefficient (S) of n-type vapor grown carbon nanofibers (CNFs) and poly(vinylidene fluoride) (PVDF) melt-mixed with 15 wt% of those CNFs is analyzed. At 40 °C, the CNFs show stable n-type character (S=−4.8 μV·K^{-1}) with an σ of *ca.*165 S·m^{-1}, while the PVDF/CNF composite film shows an σ of *ca.* 9 S·m^{-1} and near-zero S (S=−0.5 μV·K^{-1}). This experimental reduction in S is studied by the density functional tight binding (DFTB) method revealing a contact electron transfer from the CNFs to the PVDF in the interface. Moreover, in the temperature range from 40 °C to 100 °C, the $\sigma(T)$ of the CNFs and PVDF/CNF film, successfully described by the 3D variable range hopping (VRH) model, is explained as consequence of a thermally activated backscattering mechanism. On the contrary, the $S(T)$ from 40 °C to 100 °C of the PVDF/CNF film, which satisfactorily matches the model proposed for some multi-walled carbon nanotube (MWCNT) doped mats; however, it does not follow the increase in $S(T)$ found for CNFs. All these findings are presented with the aim of discerning the role of these n-type vapor grown carbon nanofibers on the σ and S of their melt-mixed polymer composites.

Keywords Carbon nanofibers; Poly(vinylidene fluoride); Seebeck coefficient; P-type doping; Density functional based tight binding; Variable range hopping

Citation: Paleo, A. J.; Serrato, V. M.; Mánuel, J. M.; Toledano, O.; Muñoz, E.; Melle-Franco, M.; Krause, B.; Pötschke, P.; Lozano, K. Doping effect of poly(vinylidene fluoride) on carbon nanofibers deduced by thermoelectric analysis of their melt mixed films. *Chinese J. Polym. Sci.* **2024**, *42*, 1802–1810.

INTRODUCTION

In the last decades, energy production has become a paramount challenge for humanity due to its increasing demand and the expected shortage of fossil fuels.[1] Thus, great effort is being made to improve the efficiency of renewable energy harvesting devices.[2] However, another way to minimize energy consumption is the use of waste heat, transforming it into electrical energy and thereby facilitating its use and transport.[3] While it is true that the use of waste heat, even if highly efficient, cannot completely replace the role of fossil fuels in energy production, it can make a decisive contribution to reducing its consumption in industry,[4] domestic heating,[5] and transport.[6] In view of the above, devices based on the thermoelectric (TE) effect,[3] in which the voltage difference ΔV induced between two electrical contacts at different temperatures ΔT can be used to produce an electrical current, are currently attracting attention among the different strategies for waste heat harnessing.[7] In practical terms, the performance of TE devices is described by their figure of merit $zT = \frac{S^2\sigma}{k}T$, which accounts for the product of the electrical conductivity σ, the squared Seebeck coefficient S, and the temperature T, divided by the thermal conductivity k.[8] In order to improve the efficiency of a TE material, the electric conductivity and Seebeck coefficient, this latter defined as $S = -\frac{\Delta V}{\Delta T}$, has to be maximized, while the thermal conductivity should be minimized.[9] It should be noticed that the Seebeck coefficient can take a positive or negative sign, depending which charge carriers are responsible for the TE effect in the cor-

* Corresponding author, E-mail: ajpaleovieito@2c2t.uminho.pt
Received April 2, 2024; Accepted July 8, 2024; Published online September 27, 2024

© Chinese Chemical Society
Institute of Chemistry, Chinese Academy of Sciences

responding material. With regard to the latter, if electrons (holes) are its main contributors, then a negative (positive) *S* is measured.[10] This is important to notice since a highly efficient TE generator requires positive (p-type) and negative (n-type) TE materials thermally coupled with a hot and cold reservoir.[11] In this respect, the TE properties of inorganic materials, such as metal alloys,[12] usually containing toxic and heavy elements like, for example, bismuth, tellurium, or lead, as well as metal oxides, ceramics and conventional semiconductors, have been investigated in recent decades.[13] Thus, for reference only, the power factor PF, defined as the product of the electrical conductivity and the square of the Seebeck coefficient, $PF = \sigma S^2$, of metallic compounds, such as the Sb-doped TiNiSn alloy have already reached values as high as 7×10^{-3} $W\cdot m^{-1}\cdot K^{-2}$.[14] However, despite the high PF, and due to their metallic nature, thermal conductivity is usually also high, leading to a decrease in their figure of merit *zT*. Accordingly, a strategy to avoid this undesired high thermal conductivity, while keeping the electrical conductivity as high as possible, is to create a composite containing an insulating polymer matrix filled with a network of electrically conducting fillers.[15] In such type of conductive polymer composites (CPCs), the thermal conductivity can be significantly lowered taking advantage on the insulating features of polymers, and the conductive nature of the filler which forms at a certain filler content a conductive network thereby surpassing the electrical percolation threshold results in significantly increased electric conductivity as compared to that of the polymer matrix.[16] Other advantages of using CPCs for TE devices are their relatively low material and processing costs, the high availability of the raw materials, the low toxicity and weight, and their excellent flexibility.[17]

Regarding the type of electrically conductive fillers used in CPCs, fillers with high aspect ratio, such as carbon nanotubes (CNTs) are favorable. Due to their high length at small diameters, low percolation thresholds with high electrical conductivities can be achieved when they are homogeneously dispersed in the polymer matrix. This means that from the intrinsic electric conductivity of the CNTs chosen, the highest electric conductivity of their CPCs can be estimated quite exactly from the volume fractions above electrical percolation threshold (ϕ_c).[18] On the contrary, very little is known about the role of insulating polymers on the *S* of final CPCs, even though it has already been reported that the interaction with the insulating polymer matrix may lead to p- or n-doping of the CNTs.[19] Therefore, understanding the mechanisms underlying the σ and *S* in this type of CPCs can help to exploit this dual doping behaviour and find CPCs with enhanced power factor.

In this context, the electrical conductivity, Seebeck coefficient, and morphological properties of poly(vinylidene difluoride) (PVDF) melt-processed film and carbon nanofibers (CNFs), a system which was previously investigated regarding its thermal and electromagnetic shielding properties,[20] are presented. CNFs have been selected as conductive fillers because their previously reported and uncommon negative *S* values,[21] while PVDF was chosen as host polymer because its strong polar nature,[22] which could affect the intrinsic n-type character of the CNFs. In this study, the $\sigma(T)$ and $S(T)$ values in the range from 40 °C to 100 °C of as-received CNFs and of a melt-mixed PVDF/CNF composite (15 wt% of CNFs) are compared and discussed. In addition, Density Functional based Tight-Binding (DFTB) simulations were performed to estimate the charge transfer between PVDF and CNF, while variable range hopping[23] and nonlinear Seebeck models[24] were employed to reproduce the $\sigma(T)$ and $S(T)$ of the as-received the CNFs and the PVDF/CNF composite film, with the final aim of improving the understanding of the physical origin of both quantities.

EXPERIMENTAL

Materials and Processing

Poly(vinylidene fluoride) (Kynar® 740 from Arkema) was applied in the shape of pellets. The carbon nanofibers (PR 24 RC AG) were supplied from Applied Sciences Inc. (Cedarville, OH, USA) and represent a non-commercial grade. These nanofibers have hollow cores and round cross-section with diameters in the range of 200 nm.[20] The CNFs and PVDF were used as received.

PVDF/CNF composite films with 15 wt% of CNFs (far above the electrical percolation threshold) were produced as described elsewhere.[20] In short, they were prepared by high shear mixing in a Haake Rheomix Polylab System using 100 r/min as rotational speed at a temperature of 210 °C for 8 min of total mixing. The polymer pellets and CNFs were alternately filled into the main hopper of the compounder. Then, composite films were formed by compression molding (Carver, Inc.,Wabash, Indiana, USA). For that, the composite batch in form of pellets was placed between two squared shaped stainless-steel plates and then pressed to approximately 10.000 psi and 210 °C for 8 min. At the end, squared films of 3.6 cm × 3.6 cm and average thickness of approximately 0.8 mm were used for characterization in this study. It is noticed that the PVDF/CNF composite film with 15 wt% of CNFs analyzed here will be referred to as the PVDF/CNF film.

Morphologic, Chemical, and Thermal Analysis

Detailed information on CNFs was obtained using transmission electron microscopy (TEM) associated techniques, namely atomically resolved or high resolution TEM (HRTEM) imaging. To this purpose, a TALOS S200 STEM microscope (ThermoFischer Scientific, Waltham, MA, USA), available at the University of Seville Research, Technology and Innovation Centre (CITIUS, University of Seville) was utilized. The electron beam was accelerated using a voltage of 200 kV, which, as far as it was observed during the experiments, produced no discernible beam damage on the fibers. The electron-transparent sample preparation, in this case, consisted, first, in obtaining a *ca*. 0.15 $g\cdot L^{-1}$ suspension of PR 24 RC AG nanofibers on partially denatured ethanol 96%. This solution was sonicated during 5 min using a VCX-750 Watt Ultrasonic Processor and a CV334 Converter (Sonics&Materials, Inc., Newtown, CT, USA). One single drop from this solution was deposited with a micropipette on a face up lacey-carbon 300 mesh cupper grid (Electron Microscopy Sciences, Hatfield, UK), which was heated at 50 °C during 24 h previous to its study under the accelerated electron beam.

Melt-mixed strands of the PVDF/CNF films were cryo-fractured in liquid nitrogen and the surface was covered with

https://doi.org/10.1007/s10118-024-3200-y

3 nm platinum before examining using a scanning electron microscope (SEM) (Ultra plus microscope, Carl Zeiss GmbH, Germany, field emission cathode) at 3 kV. Infrared measurements (FTIR, IRAffinity-1S, Shimadzu) were performed at room temperature in transmission mode from 500 cm^{-1} to 2000 cm^{-1}. FTIR spectra were collected with 40 scans and a resolution of 4 cm^{-1} at room temperature. Differential scanning calorimetry measurements (DSC) were performed in a nitrogen atmosphere using a Diamond DSC (Perkin Elmer). The specimens were heated from 30 °C to 260 °C at a rate of 10 °C·min^{-1} and isothermally maintained at 260 °C for one minute, then they were cooled down at a rate of 10 °C·min^{-1}. A second heating cycle was performed under the same conditions.

Electrical Conductivity and Seebeck Coefficient Analysis

The σ and S were carried out in a measuring device developed and constructed at IPF Dresden.[25,26] The measurements of electrical volume conductivity and thermovoltage were performed at 40, 60, 80 and 100 °C, respectively. The specimens with the size of 25 mm × 36 mm cut from the compression molded films were painted at the ends of the strips with conductive silver for improvement of the electrical contact. The measurement procedure is described in detail in Krause *et al*.[26]

Thermal Conductivity Analysis

The thermal conductivity of the PVDF/CNF film was calculated from the product of thermal diffusivity, density, and specific heat capacity. The thermal diffusivity was measured on compression moulded rectangle samples (10 mm × 10 mm, thickness 1 mm) through the plate thickness using the light flash apparatus LFA 447 NanoFlash (Netzsch-Gerätebau GmbH, Selb, Germany) at 40, 60, 80 and 100 °C. The specific heat capacity of the composites was calculated by comparing the signal heights between the composite and the reference Pyroceram 9606 (with known specific heat capacity) using the LFA 447 NanoFlash. The density of composites was determined using a buoyancy method.

Computer Modeling

In order to study the interactions and the doping between the PVDF and CNFs, Density Functional based Tight Binding (DFTB) simulations in a model system, consisting of a PVDF 16 monomer oligomer adsorbed on a hexagonal graphene flake $C_{834}H_{78}$ were performed. Thereby the DFTB+ package[27] with the DFTB3 third order parametrization developed specifically for organic systems[28] augmented with Grimme's dispersion correction[29,30] was used.

Three different thread conformations observed in crystalline phases of PVDF were modelled, namely: the all-*trans* (β-phase), the tGtG′ (where "t" stands for trans and "G" for gauche, found in the α-phase), and the tttGtttG′ configurations (γ-phase), Fig. 1. In addition, different initial orientations of the PVDF molecules were proposed considering PVDF anisotropy and minimized until forces were lower than 10^{-4} a.u., and the energy difference between consecutive geometries was smaller than 1 meV. The charge population of each atomic species was computed with the CM5 charge partition scheme present in the xTB-GFN1 methodology.[31,32]

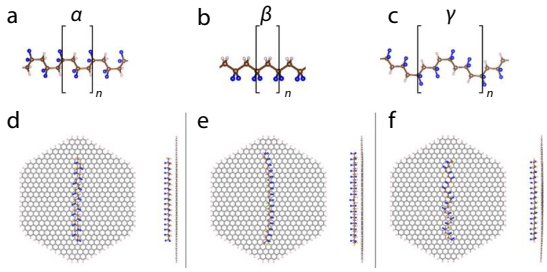

Fig. 1 Different PVDF conformations. Panel (a–c) shows the PVDF thread conformations found in α-, β-, and γ-phases, respectively. Panels (d–f) show the adsorption geometries of the molecular PVDF in tGtG′, tt, and tttGtttG′ on the graphene flake surface in their minimum energy configuration. Hydrogen and fluorine atoms are depicted in white and blue, respectively. Carbon atoms in PVDF and the graphene flake have been depicted in brown and grey respectively.

RESULTS AND DISCUSSION

Morphologic, Chemical, and Thermal Analysis

CNFs consist of cylindrical, uniform tubes, as confirmed by TEM micrographs such as the ones in Fig. 2(a). The images in this figure, obtained in HRTEM mode using a 40 μm objective aperture, show the characteristic hollow, tubular morphology of these CNFs. This can be observed more clearly at lower magnification images, such as Fig. 2(a), where the central region corresponds to a bright area of the fiber image, which is associated to a lower amount of material, as it is expected for a cavity. At high magnifications (Fig. 2b), the fibers reveal crystalline planes, as is deduced by the fringes that appear at the fiber internal surface, close to the cavity.

Fig. 3 shows representative SEM images of the cryo-fractured surface morphology of the PVDF/CNF film. A homogeneous dispersion and distribution of the CNFs throughout the PVDF is observed in Fig. 3(a). However, the absence of CNFs coated with the polymer together with the voids created by

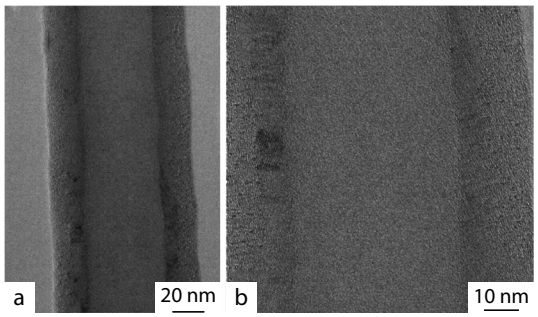

Fig. 2 Images for a representative region of a single CNF, obtained in HRTEM mode, using (a) lower of and (b) higher magnifications.

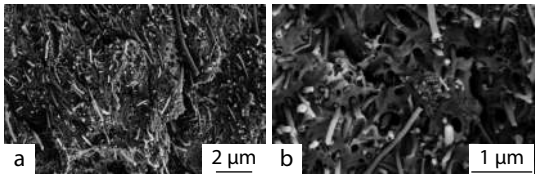

Fig. 3 SEM micrographs of the PVDF/CNF film at (a) lower and (b) higher magnifications.

https://doi.org/10.1007/s10118-024-3200-y

the CNFs pulled out from the PVDF of Fig. 3(b) indicate relatively low adhesion between the CNFs and the PVDF.

The PVDF crystal phases in the PVDF and PVDF/CNF films were analysed by FTIR (Fig. 4 and Table S1 in the electronic supplementary information, ESI). The PVDF spectrum presents bands at 760, 795 and 976 cm^{-1}, for characteristic of the α-phase.[33] It is also noticed the presence of additional bands at 842 and 1280 cm^{-1} corresponding to the β-phase, and a band at 1242 cm^{-1} as a signature of the γ-phase[34]. Details of the assignment for the rest of bands shown in Fig. 4 can be accessed at Table S1 (in ESI). The relative amount of electroactive β and γ-phases in the PVDF and PVDF/CNF films can be calculated using the following relationship:[34]

$$F_{EA} = \frac{I_{EA}}{\left(\frac{K_{840}}{K_{763}}\right) I_{763} + I_{EA}} \times 100\% \quad (1)$$

where $I_{EA} = I_{840}$ and I_{763} are the absorbencies of the respective bands, and $K_{840} = 7.7\times10^4$ $cm^2 \cdot mol^{-1}$ and $K_{763} = 6.1\times10^4 cm^2 \cdot mol^{-1}$ are the adsorption coefficients corresponding to those wavenumbers. Therefore for the neat PVDF, we can conclude that of its entire crystalline component (39.1% according to the DSC analysis discussing below) 64.4% corresponds to α-phase, while 35.6% corresponds to β and γ-phases ($F_{EA} = 35.6\%$). In order to distinguish the specific contribution for each of the electroactive β and γ-phases, the following relations can be used:[34]

$$F(\beta) = F_{EA}\left(\frac{\Delta H_\beta}{(\Delta H_\beta + \Delta H_\gamma)}\right) \quad (2)$$

$$F(\gamma) = F_{EA}\left(\frac{\Delta H_\gamma}{(\Delta H_\beta + \Delta H_\gamma)}\right) \quad (3)$$

where ΔH_β and ΔH_γ are the differences in absorbance between the bands at 1280 and 1242 cm^{-1} (characteristic of the β and γ-phases, respectively), and their nearest valleys (1260 and 1225 cm^{-1}, respectively). As it is seen in Fig. 4, the band at 1242 cm^{-1} (corresponding to γ-phase) is barely detected, so it can be deduced that the main electroactive phase for PVDF corresponds to β. In the case of the PVDF/CNF film, which shows a total crystallinity of 39.4% (according to DSC), it is noticed that, because the absorbency of the CNFs could not be decoupled from the PVDF, Eq. (1) could not be used for calculating the total amount for the electroactive β and γ-phases. However, the band at 1242 cm^{-1} is clearly formed for the PVDF/CNF film, and thus it is deduced that the CNFs have promoted also the formation of γ-phase in the PVDF/CNF film.

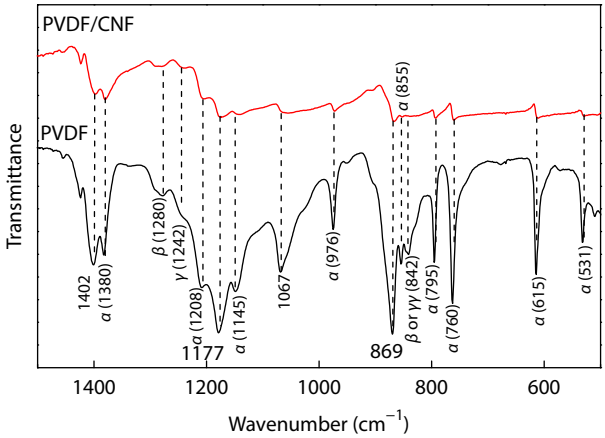

Fig. 4 FTIR spectra of the PVDF and PVDF/CNF film.

DSC analysis of the PVDF and PVDF/CNF film was also performed, and the results are shown and summarized in Fig. 5 and Table 1. It is noticed that the melting temperature (T_m), melting enthalpy (ΔH_m), crystallization temperature (T_c), and crystallization enthalpy (ΔH_c) presented here were obtained from the second heating and first cooling runs. A melting temperature and enthalpy of 168.6 °C and 40.9 $J \cdot g^{-1}$, respectively, were found for the processed PVDF. For the PVDF/CNF film, no significant changes in melting temperature and enthalpy were observed compared to the PVDF. Thus, the T_m drops from 168.6 °C to 167.0 °C, while the ΔH_m increases from 40.9 $J \cdot g^{-1}$ for the unfilled PVDF to 41.2 $J \cdot g^{-1}$ for the composite (calculated on the polymer content). In addition, the crystallization temperature of the PVDF/CNF film (134.4 °C) was 2 °C higher than the T_c of PVDF (132.4 °C). Similar shift of T_c with the addition of CNF in melt-mixed PVDF/CNF composites has been already reported,[35,36] and it has been associated to the nucleating agent effect of the CNFs in PVDF. To confirm this assertion, the degree of crystallinity (ΔX_c) in % of the PVDF and PVDF/CNF films was calculated by:

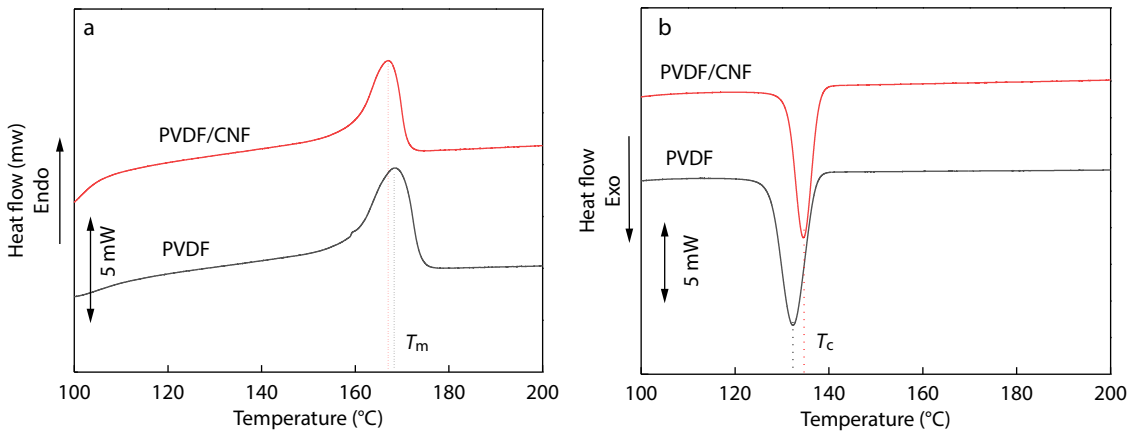

Fig. 5 DSC thermograms of (a) second heating and (b) first cooling of the PVDF and PVDF/CNF film (dotted lines indicating T_m and T_c are guides for the eyes).

https://doi.org/10.1007/s10118-024-3200-y

Table 1 DSC results from second heating and first cooling thermograms of the PVDF and PVDF/CNF film.

Sample	T_m (°C)	T_c (°C)	ΔH_m (J·g^{-1})	ΔX_c (%)
PVDF	168.6	132.4	40.9	39.1
PVDF/CNF	167.0	134.4	41.2	39.4

$$\Delta X_c = \frac{\Delta H_m}{\Delta H_0 f_{PVDF}} \times 100\% \quad (4)$$

where ΔH_m is the melting enthalpy of the PVDF and $\Delta H_0 f_{PVDF}$ is the melting enthalpy of the 100% crystalline PVDF (104.7 J·g^{-1}).[37] The degree of crystallinity increases slightly from 39.1% for PVDF to 39.4% for the PVDF/CNF film, which is attributable to the synergetic combination of the self-nucleation mechanisms promoted by the CNFs and the PVDF.[36]

In summary from DSC analysis, it is concluded that total crystalline component of PVDF/CNF film is practically the same as neat PVDF, while from FTIR is detected that CNFs promotes the formation of γ-phase.

Electrical Conductivity and Seebeck Coefficient of the CNFs and the PVDF/CNF Film at 40 °C

The electrical conductivity of the CNFs and PVDF/CNF film at 40 °C is summarized in Table 2. Quite unexpectedly, the σ (*ca.* 165 S·m^{-1}) of this CNF grade (PR 24 RC AG) is higher than the σ of *ca.* 131 S·m^{-1} at 40 °C reported for the commercial grades Pyrograf® III CNFs PR 19 LHT XT and PR 24 LHT XT,[38] and the σ of *ca.* 129 S·m^{-1} at 46 °C measured for PR 25 PS XT[39] (Table S2 in ESI). Logically, the electrical contact resistance of the as-received CNF networks should increase after the addition of the insulating PVDF, which is why the σ of the PVDF/CNF film is significantly lower (9.3 S·m^{-1}). Interestingly, this value is higher than the σ of 0.2 S·m^{-1} found for polypropylene (PP)/10 wt% CNF composites melt-processed with chemically treated CNFs (PR 24 RC AG, the same grade as used in this work).[40] Notably, the same value of 0.2 S·m^{-1} has been found for the PVDF/CNF film studied in this work, but melt-processed with lower contents of CNFs (12.5 wt%), as shown in Table S2 (in ESI). It should be noticed that higher values of 28 and 63 S·m^{-1} have been reported for melt-processed poly(ether ether ketone) (PEEK) and PP composites filled with 10 wt% and 5 wt% of Pyrograf® III CNFs (PR 24 LHT XT),[38,41] respectively. This finding matches well with the supplier´s assertion that CNFs subjected to post-processing heat treatment (LHT) and in debulked form (XT) are the perfect choice for achieving CPCs with higher values of σ.[42] Quite noticeably this value of σ (9.3 S·m^{-1}) for the PVDF/CNF film is comparable to the values of 3.2 S·m^{-1} reported for melt-processed PVDF composites filled with 2 wt% of commercial multiwall carbon nanotubes (MWCNTs) NC7000™, though higher values of 194.5 and 139.3 S·m^{-1} have been reported when PVDF was filled with 2 wt. % of MWCNTs CNS-PEG and single wall carbon nanotubes (SWCNTs) Tuball™, respectively[43] (Table S2 in ESI).

The Seebeck coefficients at 40 °C of the CNFs and PVDF/CNF film are shown in Table 2. In contrats to most CNTs, which are p-type due to their oxygen doping with the environment,[44] the CNFs used in this study have a negative *S* value of −4.8 μV·K^{-1}. However, this n-type character is to be expected since some others of the Pyrograf® III CNF grades have already been reported to exhibit negative *S* values,[38,39] associated with the resonances near the E_F at the density of states caused by impurities present in the CNF structure.[45] In addition, the *S* value is comparable to the *S* of *ca.* −5.4 μV·K^{-1} already reported for Pyrograf® III CNFs PR 19 LHT XT and PR 24 LHT XT,[38] while near-zero *S* of *ca.* −0.6 μV·K^{-1} have been found for pyrolytically stripped (PS) Pyrograf® III CNFs PR 25 PS XT[39] (Table S2 in ESI). It is therefore evident from the data presented in Table S2 that the values of σ and *S* found for this type of commercial CNFs cannot compete with those found for SWCNTs Tuball™. The *S* of the PVDF/CNF film at 40 °C (presented as red triangles in Fig. 6) also shows a negative *S* of −0.5 μV·K^{-1} (Table 2), which was slightly lower (in absolute value) than the S of −0.9 μV·K^{-1}, observed for PVDF/CNF film with 12.5 wt% of CNFs. Hence, the PVDF/CNF film maintains the n-type character of CNFs, though with a near-zero value of *S* close to the Charge Neutrality Point (CNP).[46] Notably, it should be noticed that some reduction of *S* has been found in other polymer composites melt-mixed with similar types of CNFs.[38,41]

In order to complete the thermoelectric analysis, the power factor PF ($S^2\sigma$) and the figure of merit ($zT = \frac{S^2\sigma}{k}T$) at 40 °C of the PVDF/CNF film and CNF powder were calculated, and the results are shown in Table 2. The CNF powder shows the same PF of 3.8×10^{-3} μW·m^{-1}·K^{-2} as the Pyrograf® III CNFs PR 19 LHT XT and PR 24 LHT XT materials.[38] The value is higher than the PF of 4.6×10^{-5} μW·m^{-1}·K^{-2} at 46 °C observed in Pyrograf® III CNFs PR 25 PS XT powder[39] (Table S2 in ESI). The PVDF/CNF film achieves a PF of 2.6×10^{-6} μW·m^{-1}·K^{-2}, which is lower than the PF of 1.2×10^{-3} μW·m^{-1}·K^{-2} obtained in PP/CNF composites with 5 wt% of Pyrograf® III CNFs PR 24 LHT XT,[38] and the PF of 7×10^{-4}, 1×10^{-1} and 8×10^{-2} μW·m^{-1}·K^{-2} achieved in PVDF composites with 2 wt% of MWCNTs NC7000™, CNS-PEG, and SWCNTs Tuball™, respectively[43]

Table 2 Electrical conductivity σ, Seebeck coefficient S, power factor PF, and figure of merit *zT* at 40 °C of the PVDF/CNF film and PR 24 RC AG CNF powder.

Sample	σ (S·m^{-1})	*S* (μV·K^{-1})	PF (μW·m^{-1}·K^{-2})	*zT*
PVDF/CNF	9.3±0.1	−0.5±0.01	2.6×10^{-6}	2.8×10^{-9}
CNF powder	165.1±8.5	−4.8±0.1	3.8×10^{-3}	2.8×10^{-6}

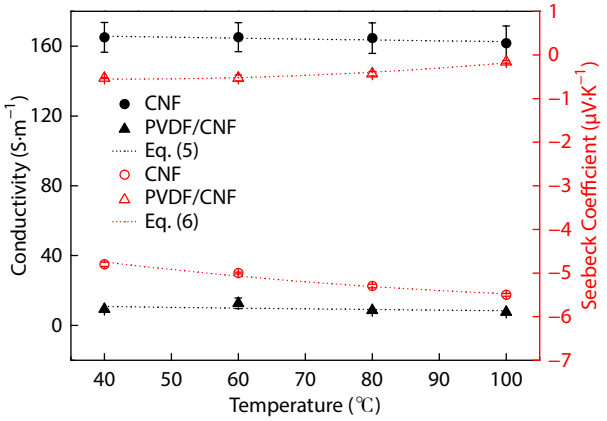

Fig. 6 Effect of temperature on the electrical volume conductivity σ (black icons) and Seebeck coefficient *S* (red icons) of the CNFs (circle icons) and PVDF/CNF film (triangle icons). (The black and red dash lines represent the fitting with Eq. (5) and Eq. (6), respectively).

(Table S2 in ESI). The *zT* at 40 °C of the CNF powder was estimated by using the thermal conductivity of 0.43 $W{\cdot}m^{-1}{\cdot}K^{-1}$ reported on anisotropic paper-like mats of Pyrograf® III CNFs,[47] while *zT* at 40 °C of PVDF/CNF film was calculated from the value of 0.29 $W{\cdot}m^{-1}{\cdot}K^{-1}$ tested as described in experimental section. The *zT* of the CNF powder presented a value of 2.8×10^{-6} (Table 2), the same as the *zT* estimated in the same way for Pyrograf® III CNFs PR 19 LHT XT and PR 24 LHT XT powders[38] (Table S2 in ESI). As expected, the PVDF/CNF film showed lower zT of 2.8×10^{-9}, which is worse than the value of 1.3×10^{-6} found for PP/CNF composites with 5 wt% of Pyrograf® III PR 24 LHT XT CNFs[38] (Table S2 in ESI). Comparatively, the zT calculated for melt-processed PVDF/CNT composites with 2 wt% of MWCNTs NC7000™, CNS-PEG, and SWCNTs Tuball™ achieved better values of 7.4×10^{-7}, 1.2×10^{-4} and 9×10^{-5}, respectively,[43] (Table S2 in ESI).

To investigate the potential doping role of PVDF on CNFs, adsorbed PVDF oligomers on an idealized external graphene CNF flake were modelled as described in experimental section. The model reveals a net flux of electrons from the graphene flake to the PVDF in all cases of *ca.* $0.01e^-$ per PVDF monomer, Table 3. This effect, if small, is able to effectively alter charge carriers' densities of CNFs. Notably, it should be noticed that a similar net flux of electrons from the graphene flake to other polymers such as PP and PEEK has also been obtained by comparable models.[18,41]

From these results, an electron-withdrawing (p-type doping) due to PVDF in contact with related nanocarbons as MWCNTs would be also expected. Confirming this, higher positive Seebeck coefficients have been reported for PVDF/MWCNT composites filled with two types of MWCNTs (*i.e.*, NC7000™ and CNS-PEG) with respect to their corresponding as-received MWCNT powders.[43] However, in the same work, the positive values of *S* for PVDF composites with 2 wt% of SWCNTs Tuball™ were lower than for the SWCNTs Tuball™ (Table S2 in ESI). Thus, it is inferred that PVDF withdraws electrons (p-type doping) to MWCNTs (as it is shown in Ref. [43]) as well as to CNFs (as it is shown in this work) while PVDF donates electrons (n-type doping) to SWCNTs (as it is shown in Ref. [43]). A hypothesis to explain this latter case is that due to the larger positive *S* value of SWCNTs Tuball™ (39.6 $\mu V{\cdot}K^{-1}$), a higher hole concentration is expected due to the oxygen (p-type doping) compared to those CNFs and MWCNTs. Therefore, it would be more difficult for PVDF to withdraw electrons from SWCNTs.

Table 3 Charge doping in graphene normalized by the number of carbon atoms of PVDF molecule computed with the CM5 partition scheme for the different PVDF conformations.

Conformation	tGtG'	tt	tttGtttG'
$\Delta q n_C^{-1}\left(\times10^{-3}e^-\right)$	(+) 5.0	(+) 5.1	(+) 4.7

Electrical Conductivity and Seebeck Coefficient of the CNFs and the PVDF/CNF Film from 40 °C to 100 °C

The electric conductivity $\sigma(T)$ of the CNFs and PVDF/CNF film in the range from 40 °C to 100 °C is shown in Fig. 6 (black icons) and Table 4. As referred previously, the σ at 40 °C of this grade (PR 24 RC AG) is about 165.1 $S{\cdot}m^{-1}$, and very small deviations to this value are observed when increasing the temperature up to 80 °C. However, beyond 80 °C, the σ reduces from *ca.* 164.6 $S{\cdot}m^{-1}$ (80 °C) to *ca.* 161.7 $S{\cdot}m^{-1}$ at 100 °C. Notably, a similar behaviour for $\sigma(T)$ was found for Pyrograf® III CNFs PR 19 LHT XT powders in the same interval.[38] Thereby for these temperatures, and as in the case of Pyrograf® III CNFs PR 19 LHT XT, PR 24 LHT XT[38] and PR 25 PS XT,[39] the $\sigma(T)$ of this non-commercial grade shows a positive temperature coefficient (PTC) effect, which is defined as an increase in electrical resistivity when the material is subjected to an increase in temperature. Also the $\sigma(T)$ of the PVDF/CNF film shows a PTC effect. In particular, σ increases first from *ca.* 9.3 $S{\cdot}m^{-1}$ (40 °C) to *ca.* 12.6 $S{\cdot}m^{-1}$ at 60 °C, and then drops from *ca.* 8.6 $S{\cdot}m^{-1}$ (80 °C) to *ca.* 7.6 $S{\cdot}m^{-1}$ at 100 °C. It is noticed that the same PTC effect was found in the PP/CNF composites with 5 wt% of Pyrograf® III CNFs PR 24 LHT XT and PR 19 LHT XT.[38] Nevertheless, this finding differs from previous work,[41] where the $\sigma(T)$ of the PEEK/CNF composites with 10 wt% of Pyrograf® III CNFs PR 24 LHT XT remained practically constant within the same interval of temperatures.

Fig. 6 (red icons) and Table 4 introduce the $S(T)$ of the CNFs and PVDF/CNF film in the range from 40 °C to 100 °C. The first thing to notice is that the $S(T)$ of the CNFs remains negative at all temperatures with an *S* of *ca.* $-4.8\ \mu V{\cdot}K^{-1}$ at 40 °C, which changes to *ca.* $-5.5\ \mu V{\cdot}K^{-1}$ at 100° C (Table 4). It has to be noticed that this increase of S (in absolute value) with the rise of temperature (from 40 °C to 100 °C) was also observed for Pyrograf® III CNFs grades (PR 25 PS XT,[39] PR 24 LHT XT and PR 19 LHT XT.[38]) On the contrary, the $S(T)$ of the PVDF/CNF film (red triangle icons) is more closely aligned to the CNP, by decreasing its Seebeck coefficient from *ca.* $-0.5\ \mu V{\cdot}K^{-1}$ (40 °C) to *ca.* $-0.2\pm0.1\ \mu V{\cdot}K^{-1}$ at 100 °C (Table 4). Therefore, the $S(T)$ of the PVDF/CNF film does not follow the $S(T)$ of the CNF powder, and it differs from the $S(T)$ observed for PP/CNF compos-

Table 4 Effect of temperature on the thermoelectric properties of the CNFs and PVDF/CNF film (*zT* of CNF estimated by using the thermal conductivity of 0.43 $W{\cdot}m^{-1}{\cdot}K^{-1}$ reported on anisotropic paper-like mats of of Pyrograf® III CNFs[47]).

T (°C)	Sample	Conductivity ($S{\cdot}m^{-1}$)	Seebeck ($\mu V{\cdot}K^{-1}$)	Power factor ($\mu W{\cdot}m^{-1}{\cdot}K^{-2}$)	Thermal conductivity ($W{\cdot}m^{-1}{\cdot}K^{-1}$)	*zT*
40	CNF	165.11±8.54	−4.80±0.05	3.8×10^{-3}		2.8×10^{-6}
	PVDF/CNF	9.31±0.07	−0.53±0.01	2.6×10^{-6}	0.29±0.02	2.8×10^{-9}
60	CNF	165.14±8.30	−5.04±0.02	4.2×10^{-3}		3.3×10^{-6}
	PVDF/CNF	12.63±3.01	−0.53±0.07	3.5×10^{-6}	0.30±0.03	3.9×10^{-9}
80	CNF	164.62±8.75	−5.28±0.04	4.6×10^{-3}		3.8×10^{-6}
	PVDF/CNF	8.66±0.37	−0.43±0.05	1.6×10^{-6}	0.31±0.03	1.8×10^{-9}
100	CNF	161.70±9.93	−5.52±0.03	4.9×10^{-3}		4.3×10^{-6}
	PVDF/CNF	7.58±0.57	−0.16±0.03	1.9×10^{-7}	0.30±0.02	2.6×10^{-10}

https://doi.org/10.1007/s10118-024-3200-y

ites with 5 wt% of Pyrograf® III CNFs PR 24 LHT XT and PR 19 LHT XT.[38] It also differs from the $S(T)$ measured for PEEK/CNF composites with 10 wt.% of Pyrograf® III CNFs PR 24 LHT XT.[41] This latter finding could be understood by the change from a one-band model for the CNFs to a two-band model for the PVDF/CNF film.[48] In the case of the CNFs, the majority charge carriers (e^-), located mainly in the conduction band, would lead to an n-type system with an increase of the S value with temperature. However, in the case of the PVDF/CNF film, where the number of e^- and holes are practically the same because the electron donation from the CNFs to the PVDF above commented, the existence of more holes in the conduction band would imply the slight decrease in $S(T)$ (absolute value) which is experimentally observed.

The power factor PF as function of temperature of the CNFs and PVDF/CNF film is shown in Table 4. The CNFs present a PF of *ca*. 3.8×10^{-3} μW·m^{-1}·K^{-2} (at 40 °C), which increases up to *ca*. 4.9×10^{-3} μW·m^{-1}·K^{-2} at 100 °C. It is noticed that the same increase was already observed for Pyrograf® III CNFs grades PR 24 LHT XT and PR 19 LHT XT, where the PF rises up to *ca*. 4.3×10^{-3} μW·m^{-1}·K^{-2} at 100 °C,[38] while for PR 25 PS XT CNFs, the PF changes from *ca*. 4.6×10^{-5} μW·m^{-1}·K^{-2} (at 46 °C) to *ca*. 7.2×10^{-5} μW·m^{-1}·K^{-2} at 100 °C.[39] In contrast, the PF of the PVDF/CNF film drops from 2.6×10^{-6} μW·m^{-1}·K^{-2} at 40 °C to 1.9×10^{-7} μW·m^{-1}·K^{-2} at 100 °C (Table 4), associated with the decrease of its S (absolute value) with temperature discussed previously. Ultimately, this corresponds to a zT of *ca*. 2.8×10^{-9} at 40 °C for the PVDF/CNF film, which diminishes up to *ca*. 2.6×10^{-10} at 100 °C.

Electronic Modeling of the CNFs and PVDF/CNF film

To complete the electrical conductivity analysis, the 3D variable range hopping (VRH) model is applied on the CNFs and the PVDF/CNF film:[23]

$$\sigma(T) = e^{\pm\left(\frac{|W_D|}{k_B T}\right)^{1/4}} \quad (5)$$

where $\frac{|W_D|}{k_B}$ is defined by the average energy potential barrier ($W_D < 0$) or potential well ($W_D > 0$), and k_B is the Boltzmann´s constant. It is noticed that if $W_D > 0$, (*i.e.*, negative exponent in Eq. 5), $\sigma(T)$ describes a thermally activated hopping mechanism across a random network of potential wells leading to $d\sigma/dT > 0$, while when $W_D < 0$, (*i.e.*, positive exponent in Eq. 5), $\sigma(T)$ is interpreted as a thermally activated backscattering mechanism across a random distribution of impurities or structural defects, leading to $d\sigma/dT < 0$.[23] It is found that the W_D of the PVDF/CNF film (−31.5 eV) is negative, as it is that of the CNFs, although the latter with much lower value of W_D (-1.6×10^{-4} eV). It has to be noticed that similar negatives W_D values of -7.7×10^{-3} and -3.3×10^{-5} eV have been reported for Pyrograf® III CNFs grades PR 19 LHT XT[38] and PR 25 PS XT,[39] respectively, while higher W_D values of −0.15 eV were found for Pyrograf® III CNFs grades PR 24 LHT XT.[38] Similarly, negative W_D values of −6.3 and −3.9 eV have been reported for melt-processed PP composites filled with 5 wt% of Pyrograf® III CNFs PR 19 LHT XT and PR 24 LHT XT, respectively.[38] Consequently, the CNFs and the PVDF/CNF film present negative W_D, so that their $\sigma(T)$ is described by the thermally activated backscattering mechanism.[49]

To understand better the $S(T)$ for the CNFs and PVDF/CNF film obtained in previous section, the model proposed for describing the nonlinear Seebeck of doped MWCNTs mats is used:[24]

Table 5 Parameters b, c, T_P and $E_P - E_F$ obtained by fitting the experimental values of $S(T)$ with Eq. (6).

Sample	b (μV·K^{-2})	c (μV)	T_p (K)	$E_p - E_F$ (eV)
CNF	3.2×10^{-3}	-1.7×10^{4}	1062.6	9.2×10^{-2}
PVDF/CNF	2.0×10^{-2}	-1.8×10^{4}	1007.5	8.7×10^{-2}

$$S(T) = bT + \frac{cT_P}{T^2}\frac{\exp\left(\frac{T_P}{T}\right)}{\left[\exp\left(\frac{T_P}{T}\right)+1\right]^2} \quad (6)$$

where bT represents the metallic (linear) term of $S(T)$, c is a constant, $T_p = (E_p - E_F)/k_B$ with E_F is the Fermi energy level, and E_P is the energy corresponding to the sharply varying and localized states near E_F in the density of states due to the contribution of impurities.[50] All the parameters b, c, T_P and $E_P - E_F$ obtained by Eq. (6) for the CNFs and PVDF/CNF film in the interval from 40 °C to 100 °C are presented in Table 5. As it can be seen, the term b of the CNFs is positive with a value of 3.2×10^{-3} μV·K^{-2}, while the T_P is 1062.6 K, yielding $E_P - E_F$ of 9.2×10^{-2} eV. Thus, the b, T_P and $E_P - E_F$ found for CNFs used here (PR 24 RC AG) are similar to the b, T_P and $E_P - E_F$ calculated by the same model for Pyrograf® III CNFs PR 19 LHT XT and PR 24 LHT XT[38] and PR 25 PS XT.[39] In addition, the $S(T)$ of the PVDF/CNF film is also fitted by Eq. (6), which yields values of b=2.0×10^{-2} μV·K^{-2}, T_p=1007.5 K and $E_p - E_F$=8.7×10^{-2} eV. It has to be noticed that the negative sign of c found in the CNFs and PVDF/CNF film can be interpreted as the resonances near the E_F at the density of states caused by impurities or defects present in the CNF structure.[24] Thus, these results, along with the negative W_D values found from Eq. (5), imply that the defects/impurities of the CNFs are the main contributors to the type of electrical transport, and negative Seebeck coefficient observed in the melt-mixed PVDF/CNF film.

CONCLUSIONS

Melt-mixed PVDF films with 15 wt% of as-received vapor grown carbon nanofibers (CNFs) were morphologically, chemically, and thermally analysed using SEM, FTIR, and DSC methods. DSC analysis shows that total crystalline component of PVDF/CNF film is practically the same as neat PVDF, while from FTIR is detected that CNFs promotes the formation of γ-phase. Further, the effect of temperature on the electrical conductivity (σ) and Seebeck coefficient (S) of the n-type CNFs and their PVDF/CNF composite in the interval from 40 °C to 100 °C was measured and elucidated using the 3D variable range hopping (VRH) model, and the model proposed for some doped multiwall carbon nanotube (MWCNT) mats. From them, it is concluded that the thermally activated backscattering mechanism produced by the structural defects or impurities of the CNFs drives the $\sigma(T)$ and $S(T)$ observed in both, the CNFs and PVDF/CNF film. In addition, electron transfer from the CNFs to the PVDF matrix which was computed using a density functional based tight binding (DFTB) Hamiltonian for an idealized model of a PVDF/CNF interface, could be the responsible for the near-zero Seebeck coefficient measured for the PVDF/CNF film in this temperature

range. The aim of the authors is that the analysis and modelling presented here help to understand the role of this type of CNFs on the electrical transport, and Seebeck coefficient found in their melt-mixed PVDF/CNF film composites.

Conflict of Interests

The authors declare no interest conflict.

Electronic Supplementary Information

Electronic supplementary information (ESI) is available free of charge in the online version of this article at http://doi.org/10.1007/s10118-024-3200-y.

Data Availability Statement

The data that support the findings of this study are available on request from the corresponding author upon reasonable request. The author's contact information: ajpaleovieito@2c2t.uminho.pt.

ACKNOWLEDGMENTS

This work was financially supported by the European Regional Development Fund through the Operational Competitiveness Program and the National Foundation for Science and Technology of Portugal (FCT) (No. UID/CTM/00264/2020 of Centre for Textile Science and Technology (2C2T) on its components Base and programmatic). A. J. P acknowledges support from project GreenAuto-Green Innovation for the Automotive Industry -PPS 3-Technical Textiles for the vehicle (Ref[a] C6448637037-00000013) financed by EU funds, through the Plano de Recuperação e Resiliência (PRR), managed by IAPMEI, I.P.- Agência para a Competitividade e Inovação. M.M.-F. and O.T. acknowledge support within the scope of the project CICECO-Aveiro Institute of Materials, UIDB/50011/2020, UIDP/50011/2020 & LA/P/0006/2020, financed by national funds through the FCT/MCTES (PIDDAC). O.T. also acknowledges support from the Spanish Ministry of Universities with European Union funds – Next Generation EU through a Margarita Salas fellowship. K.L. also acknowledges support received from National Science Foundation under PREM award DMR 2122178. The authors would like to thank the staff of the Research Technology Department of the IPF for their support in setting up the thermoelectric measuring system, Manuela Heber (IPF) for SEM imaging and Ulrike Jentzsch-Hutschenreuther (IPF) for carrying out the thermoelectric measurements.

REFERENCES

1 Ahmad, T.; Zhang, D. A critical review of comparative global historical energy consumption and future demand: the story told so far. *Energy Rep.* **2020**, *6*, 1973–1991.
2 Østergaard, P. A.; Duic, N.; Noorollahi, Y.; Kalogirou, S. Renewable energy for sustainable development. *Renewable Energy* **2022**, *199*, 1145–1152.
3 Bell, L. E. Cooling, heating, generating power, and recovering waste heat with thermoelectric systems. *Science* **2008**, *321*, 1457–1461.
4 Xu, Z. Y.; Wang, R. Z.; Yang, C. Perspectives for low-temperature waste heat recovery. *Energy* **2019**, *176*, 1037–1043.
5 El Hage, H.; Ramadan, M.; Jaber, H.; Khaled, M.; Olabi, A. G. A short review on the techniques of waste heat recovery from domestic applications. *Energy Sources, Part A: Recovery, Utilization, and Environmental Effects* **2020**, *42*, 3019–3034.
6 Lion, S.; Vlaskos, I.; Taccani, R. A review of emissions reduction technologies for low and medium speed marine Diesel engines and their potential for waste heat recovery. *Energy Conv. Manag.* **2020**, *207*, 112553.
7 Loni, R.; Najafi, G.; Bellos, E.; Rajaee, F.; Said, Z.; Mazlan, M. A review of industrial waste heat recovery system for power generation with Organic Rankine Cycle: Recent challenges and future outlook. *J. Cleaner Prod.* **2021**, *287*, 125070.
8 Mehdizadeh Dehkordi, A.; Zebarjadi, M.; He, J.; Tritt, T. M. Thermoelectric power factor: Enhancement mechanisms and strategies for higher performance thermoelectric materials. *Mater. Sci. Eng.: R: Rep.* **2015**, *97*, 1–22.
9 Hamid Elsheikh, M.; Shnawah, D. A.; Sabri, M. F. M.; Said, S. B. M.; Haji Hassan, M.; Ali Bashir, M. B.; Mohamad, M. A review on thermoelectric renewable energy: principle parameters that affect their performance. *Renew. Sustain. Energy Rev.* **2014**, *30*, 337–355.
10 Crispin, X. Thermoelectrics: carbon nanotubes get high. *Nat. Energy* **2016**, *1*, 16037.
11 He, W.; Zhang, G.; Zhang, X.; Ji, J.; Li, G.; Zhao, X. Recent development and application of thermoelectric generator and cooler. *Appl. Energy* **2015**, *143*, 1–25.
12 Sootsman, J. R.; Chung, D. Y.; Kanatzidis, M. G. New and old concepts in thermoelectric materials. *Angew. Chem. Int. Ed.* **2009**, *48*, 8616–8639.
13 Tan, G.; Zhao, L.-D.; Kanatzidis, M. G. Rationally designing high-performance bulk thermoelectric materials. *Chem. Rev.* **2016**, *116*, 12123–12149.
14 Bhattacharya, S.; Pope, A. L.; Littleton, R. T., IV; Tritt, T. M.; Ponnambalam, V.; Xia, Y.; Poon, S. J. Effect of Sb doping on the thermoelectric properties of Ti-based half-Heusler compounds, $TiNiSn_{1-x}Sb_x$. *Appl. Phys. Lett.* **2000**, *77*, 2476–2478.
15 Yu, C.; Kim, Y. S.; Kim, D.; Grunlan, J. C. Thermoelectric behavior of segregated-network polymer nanocomposites. *Nano Lett.* **2008**, *8*, 4428–4432.
16 Dang, Z. M.; Lin, Y. H.; Nan, C. W. Novel ferroelectric polymer composites with high dielectric constants. *Adv. Mater.* **2003**, *15*, 1625–1629.
17 Han, S.; Chen, S.; Jiao, F. Insulating polymers for flexible thermoelectric composites: a multi-perspective review. *Compos. Commun.* **2021**, *28*, 100914.
18 Paleo, A. J.; Krause, B.; Cerqueira, M. F.; Melle-Franco, M.; Pötschke, P.; Rocha, A. M. Thermoelectric properties of polypropylene carbon nanofiber melt-mixed composites: exploring the role of polymer on their Seebeck coefficient. *Polym. J.* **2021**, *53*, 1145–1152.
19 Kröning, K.; Krause, B.; Pötschke, P.; Fiedler, B. Nanocomposites with p- and n-type conductivity controlled by type and content of nanotubes in thermosets for thermoelectric applications. *Nanomaterials* **2020**, *10*, 1144.
20 Serrato, V. M.; Padilla, V.; Jones, D.; Herrera, S.; Campos, L.; Serrato III, I.; Foltz, H.; Lozano, K. Electromagnetic interference shielding effectiveness of compression molded carbon nanofiber-reinforced polyvinylidene difluoride film. *Polym. Compos.* **2023**, *44*, 592–608.
21 Paleo, A. J.; Vieira, E. M. F.; Wan, K.; Bondarchuk, O.; Cerqueira, M. F.; Goncalves, L. M.; Bilotti, E.; Alpuim, P.; Rocha, A. M. Negative

thermoelectric power of melt mixed vapor grown carbon nanofiber polypropylene composites. *Carbon* **2019**, *150*, 408–416.
22 Saxena, P.; Shukla, P. A comprehensive review on fundamental properties and applications of poly(vinylidene fluoride) (PVDF). *Adv. Compos. Hybrid Mater.* **2021**, *4*, 8–26.
23 Mott, N. F. Conduction in glasses containing transition metal ions. *J. Non-Crystalline Solids* **1968**, *1*, 1–17.
24 Choi, Y. M.; Lee, D. S.; Czerw, R.; Chiu, P. W.; Grobert, N.; Terrones, M.; Reyes-Reyes, M.; Terrones, H.; Charlier, J. C.; Ajayan, P. M.; Roth, S.; Carroll, D. L.; Park, Y. W. Nonlinear behavior in the thermopower of doped carbon nanotubes due to strong, localized states. *Nano Lett.* **2003**, *3*, 839–842.
25 Jenschke, W.; Ullrich, M.; Krause, B.; Pötschke, P. Messanlage zur Untersuchung des Seebeck-Effektes in Polymermaterialien. *tm - Technisches Messen* **2020**, *87*, 495–503.
26 Krause, B.; Pötschke, P. Polyethylene glycol as additive to achieve N-conductive melt-mixed polymer/carbon nanotube composites for thermoelectric application. *Nanomaterials* **2022**, *12*, 3812.
27 Hourahine, B.; Aradi, B.; Blum, V.; Bonafé, F.; Buccheri, A.; Camacho, C.; Cevallos, C.; Deshaye, M. Y.; Dumitrică, T.; Dominguez, A.; Ehlert, S.; Elstner, M.; van der Heide, T.; Hermann, J.; Irle, S.; Kranz, J. J.; Köhler, C.; Kowalczyk, T.; Kubař, T.; Lee, I. S.; Lutsker, V.; Maurer, R. J.; Min, S. K.; Mitchell, I.; Negre, C.; Niehaus, T. A.; Niklasson, A. M. N.; Page, A. J.; Pecchia, A.; Penazzi, G.; Persson, M. P.; Řezáč, J.; Sánchez, C. G.; Sternberg, M.; Stöhr, M.; Stuckenberg, F.; Tkatchenko, A.; Yu, V. W.-z.; Frauenheim, T. DFTB+, a software package for efficient approximate density functional theory based atomistic simulations. *J. Chem. Phys.* **2020,** *152*.
28 Gaus, M.; Goez, A.; Elstner, M. Parametrization and benchmark of DFTB3 for organic molecules. *J. Chem. Theory Comput.* **2013**, *9*, 338–354.
29 Grimme, S.; Antony, J.; Ehrlich, S.; Krieg, H. A consistent and accurate ab initio parametrization of density functional dispersion correction (DFT-D) for the 94 elements H-Pu. *J. Chem. Phys*. **2010,** *132*.
30 Grimme, S.; Ehrlich, S.; Goerigk, L. Effect of the damping function in dispersion corrected density functional theory. *J. Comput. Chem.* **2011**, *32*, 1456–1465.
31 Grimme, S.; Bannwarth, C.; Shushkov, P. A robust and accurate tight-binding quantum chemical method for structures, vibrational frequencies, and noncovalent interactions of large molecular systems parametrized for all spd-block elements (Z = 1–86). *J. Chem. Theory Comput.* **2017**, *13*, 1989–2009.
32 Marenich, A. V.; Jerome, S. V.; Cramer, C. J.; Truhlar, D. G. Charge Model 5: an extension of hirshfeld population analysis for the accurate description of molecular interactions in gaseous and condensed phases. *J. Chem. Theory Comput.* **2012**, *8*, 527–541.
33 Boccaccio, T.; Bottino, A.; Capannelli, G.; Piaggio, P. Characterization of PVDF membranes by vibrational spectroscopy. *J. Membr. Sci.* **2002**, *210*, 315–329.
34 Cai, X.; Lei, T.; Sun, D.; Lin, L. A critical analysis of the *α*, *β* and *γ* phases in poly(vinylidene fluoride) using FTIR. *RSC Adv.* **2017**, *7*, 15382–15389.
35 Vidhate, S.; Shaito, A.; Chung, J.; D'Souza, N. A. Crystallization, mechanical, and rheological behavior of polyvinylidene fluoride/carbon nanofiber composites. *J. Appl. Polym. Sci.* **2009**, *112*, 254–260.
36 Sun, L.; Wu, N.; Peng, R. Negative dielectric permittivity of PVDF nanocomposites induced by carbon nanofibers and polymer crystallization. *J. Appl. Polym. Sci.* **2020**, *137*, 49582.
37 Liu, J.; Lu, X.; Wu, C. Effect of preparation methods on crystallization behavior and tensile strength of poly(vinylidene fluoride) membranes. *Membranes* **2013**, *3*, 389–405.
38 Paleo, A. J.; Krause, B.; Mendes, A. R.; Tavares, C. J.; Cerqueira, M. F.; Muñoz, E.; Pötschke, P. Comparative thermoelectric properties of polypropylene composites melt-processed using Pyrograf®III carbon nanofibers. *J. Compos. Sci.* **2023**, *7*, 173.
39 Paleo, A. J.; Krause, B.; Cerqueira, M. F.; González-Domínguez, J. M.; Muñoz, E.; Pötschke, P.; Rocha, A. M. Thermoelectric properties of cotton fabrics dip-coated in pyrolytically stripped Pyrograf® III carbon nanofiber based aqueous inks. *Materials* **2023**, *16*, 4335.
40 Aldica, G. V.; Ciurea, M. L.; Chipara, D. M.; Lepadatu, A. M.; Lozano, K.; Stavarache, I.; Popa, S.; Chipara, M. Isotactic polypropylene-vapor grown carbon nanofibers composites: electrical properties. *J. Appl. Polym. Sci.* **2017**, *134*, 45297.
41 Paleo, A. J.; Krause, B.; Soares, D.; Melle-Franco, M.; Muñoz, E.; Pötschke, P.; Rocha, A. M. Thermoelectric properties of n-type poly(ether ether ketone)/carbon nanofiber melt-processed composites. *Polymers* **2022**, *14*, 4803.
42 Paleo, A. J.; Sencadas, V.; van Hattum, F. W. J.; Lanceros-Méndez, S.; Ares, A. Carbon nanofiber type and content dependence of the physical properties of carbon nanofiber reinforced polypropylene composites. *Polym. Eng. Sci.* **2014**, *54*, 117–128.
43 Krause, B.; Barbier, C.; Levente, J.; Klaus, M.; Pötschke, P. Screening of different carbon nanotubes in melt-mixed polymer composites with different polymer matrices for their thermoelectrical properties. *J. Compos. Sci.* **2019**, *3*, 106.
44 Bradley, K.; Jhi, S. H.; Collins, P. G.; Hone, J.; Cohen, M. L.; Louie, S. G.; Zettl, A. Is the intrinsic thermoelectric power of carbon nanotubes positive. *Phys. Rev. Lett.* **2000**, *85*, 4361–4364.
45 Paleo, A. J.; Krause, B.; Cerqueira, M. F.; Muñoz, E.; Pötschke, P.; Rocha, A. M. Nonlinear thermopower behaviour of n-type carbon nanofibres and their melt mixed polypropylene composites. *Polymers* **2022,** *14*.
46 Gusev, G. M.; Olshanetsky, E. B.; Kvon, Z. D.; Mikhailov, N. N.; Dvoretsky, S. A.; Portal, J. C. Quantum hall effect near the charge neutrality point in a two-dimensional electron-hole system. *Phys. Rev. Lett.* **2010**, *104*, 166401.
47 Mahanta, N. K.; Abramson, A. R.; Lake, M. L.; Burton, D. J.; Chang, J. C.; Mayer, H. K.; Ravine, J. L. Thermal conductivity of carbon nanofiber mats. *Carbon* **2010**, *48*, 4457–4465.
48 Liu, R.; Ge, Y.; Wang, D.; Shuai, Z. Understanding the temperature dependence of the seebeck coefficient from first-principles band structure calculations for organic thermoelectric materials. *CCS Chem.* **2021**, *3*, 1477–1483.
49 Paleo, A. J.; Krause, B.; Cerqueira, M. F.; Muñoz, E.; Pötschke, P.; Rocha, A. M. Electronic features of cotton fabric e-textiles prepared with aqueous carbon nanofiber inks. *ACS Appl. Eng. Mater.* **2023**, *1*, 122–131.
50 Mahan, G. D. Impurity resonances in carbon nanotubes. *Phys. Rev. B* **2004**, *69*, 125407.

https://doi.org/10.1007/s10118-024-3200-y